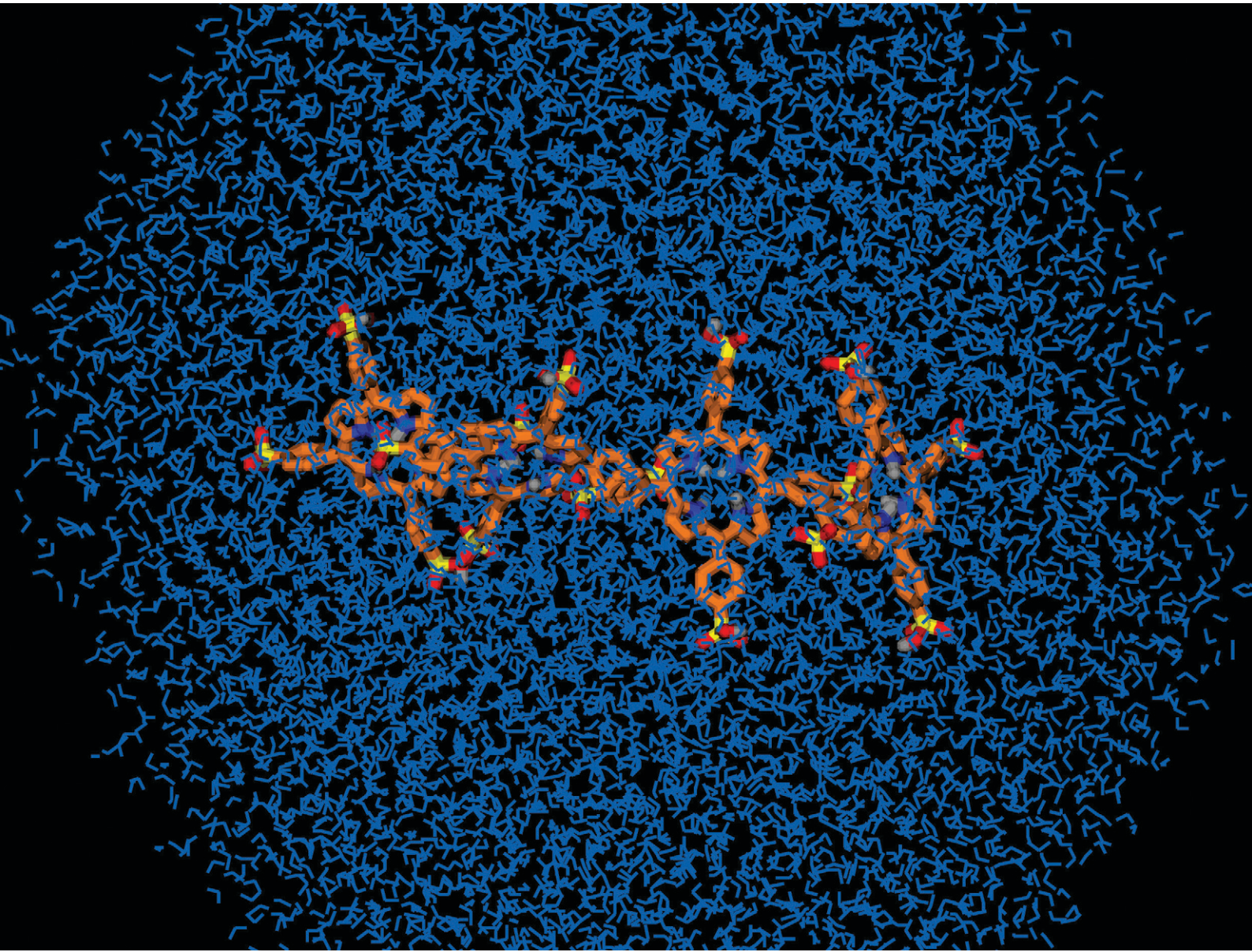


# MSDE

Molecular Systems Design & Engineering

[rsc.li/molecular-engineering](http://rsc.li/molecular-engineering)



ISSN 2058-9689

## PAPER

Laura Balulyte *et al.*  
Origins of curvature in *meso*-tetra(4-sulfonatophenyl)  
porphine aggregation: molecular dynamics and  
electronic spectroscopy



Cite this: *Mol. Syst. Des. Eng.*, 2025, 10, 635

## Origins of curvature in meso-tetra(4-sulfonatophenyl) porphine aggregation: molecular dynamics and electronic spectroscopy†

Laura Baliulyte, <sup>a</sup> Eimantas Urnietzius, <sup>a</sup> Vytautas Bubilaitis, <sup>a</sup> Mindaugas Macernis, <sup>a</sup> Lorenzo Cupellini <sup>b</sup> and Darius Abramavicius <sup>a</sup>

meso-Tetra(4-sulfonatophenyl) porphine (TPPS<sub>4</sub>) is a significant theranostic agent for photodynamic therapy (PDT) and a model system of molecular nanowires. The zwitterionic forms of TPPS<sub>4</sub> tend to form large chiral nanotubes in acidic conditions at pH ≈ 1. However, it is still not clear how these aggregates are structured at the molecular level. We describe a computational strategy to model the TPPS<sub>4</sub> aggregation of small clusters using a molecular dynamics (MD) approach. Two possible forms of zwitterionic TPPS<sub>4</sub> tetramers were considered, and their absorption and circular dichroism (CD) spectra were calculated using the Frenkel exciton model. Possible molecular packing is suggested as a candidate for the formation of large aggregates.

Received 28th January 2025,  
Accepted 20th May 2025

DOI: 10.1039/d5me00010f  
rsc.li/molecular-engineering

### Design, System, Application

Synthetic tubular porphyrin nano-aggregates are potential candidates for quantum energy wiring as well as drug-driving components in photodynamic therapy in cancer treatment. Only small molecular systems, mostly dimers, can be optimized by, *e.g.*, density functional approach with sufficient accuracy. To consider large numbers of molecules in various designs, we used the classical molecular mechanics (MM) approach, which is computationally much less expensive. The general Amber force field (GAFF) has parameters for most organic molecules; however, the parameters must be revised due to the conjugation of C=C bonds in porphyrins. Reparameterization of the zwitterionic TPPS<sub>4</sub> porphyrins is performed (leading to extension of GAFF force field parameters for porphyrin macrocycles), then tetramers are designed, solvated in a box of water. MD simulation was performed and a room temperature trajectory is obtained, which shows the emergence of global tetramer structure curling. This demonstrates the origin of tubular structure formation. Tetramer absorption and circular dichroism spectra were calculated using the Frenkel exciton model and peak positions in absorption spectra are similar to peak positions in experimentally measured spectra. From this information we can learn about various artificial chiral molecular aggregate formation for specific applications.

## Introduction

In the past few decades, aggregates of molecular pigments have been extensively investigated as potential light harvesters<sup>1</sup> and light energy concentrators.<sup>2</sup> Water-soluble, metal-free, highly stable aggregates are additionally important as possible theranostic agents for photoacoustic imaging (PAI) and photodynamic therapy (PDT) due to the intense light absorption in the phototherapeutic window.<sup>3</sup> A graphical representation of the curved TPPS<sub>4</sub> tetramer in a water box, illustrating light absorption and the generation of optical spectra, is shown in Fig. 1.

<sup>a</sup> Institute of Chemical Physics, Faculty of Physics, Vilnius University, Sauletekio av. 9, LT-10222 Vilnius, Lithuania. E-mail: laura.baliulyte@ff.vu.lt

<sup>b</sup> Department of Chemistry and Industrial Chemistry, University of Pisa, 56124, Pisa, Italy

† Electronic supplementary information (ESI) available. See DOI: <https://doi.org/10.1039/d5me00010f>

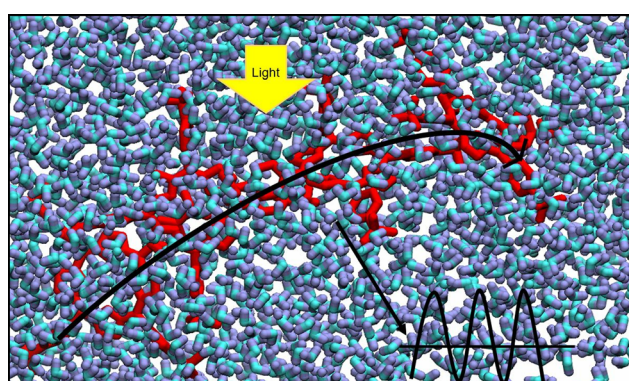


**Fig. 1** A graphical representation of the TPPS<sub>4</sub> tetramer light absorption and optical spectra generation. The photosensitizer (TPPS<sub>4</sub> tetramer) is irradiated with light and the resulting optical spectra, which can be measured with a spectrometer, are shown.



PDT is an innovative and non-invasive form of treatment of oncological diseases. PDT is also well tolerated by patients because it has high selectivity for neoplastic tissues.<sup>4</sup> In contrast, many cancer patients who undergo chemotherapy<sup>5</sup> and radiotherapy<sup>6</sup> experience side effects. 5,10,15,20-Tetrakis(4-sulfonatophenyl) porphyrin (TPPS<sub>4</sub>) molecules absorb light and may initiate the activation processes leading to the death of tumor cells, hence could be used in PDT.<sup>3</sup> PDT treatment success might be related to aggregation and spectroscopic characteristics. However, the structural details of TPPS<sub>4</sub> aggregation are still not completely understood.

The prevalent protonation state of TPPS<sub>4</sub> molecules depends on the pH of the solvent: H<sub>3</sub>TPPS<sub>4</sub><sup>2+</sup> (dicationic form) is prevalent at extremely low pH (<0), H<sub>6</sub>TPPS<sub>4</sub><sup>0</sup> (zwitterionic form) appears to dominate at pH ≈1, whereas H<sub>4</sub>TPPS<sub>4</sub><sup>2-</sup> (diacid form) dominates in the pH ≈3 to 4 range, and H<sub>2</sub>TPPS<sub>4</sub><sup>4-</sup> (tetra-anion form) dominates in neutral (pH ≈7) and alkaline (pH ≈12) solutions.<sup>7,8</sup> The monomers of TPPS<sub>4</sub> spontaneously associate into tubular structures – J-aggregates (side by side) and/or H-aggregates (face to face) – in the host solution, depending on the pH value of the aqueous medium and on the concentration of TPPS<sub>4</sub> molecules.<sup>9,10</sup> The structures of TPPS<sub>4</sub> could be helical,<sup>11</sup> flat or flocculated,<sup>12</sup> but there is still little knowledge about the explicit molecular packing.

J-type aggregates are formed when monomers concentrate with respect to each other in a direction approximately parallel to the molecular plane, while H-aggregates are formed when the monomers are placed on top of each other.<sup>13</sup> The self-organization state of molecules can be deduced from the changes in spectral properties of the solution samples. J-aggregates are characterized by a bathochromic (red-shifted) absorption band, whereas H-aggregates possess a hypsochromic (blue-shifted) absorption band in relation to the monomer absorption band.<sup>14</sup> It has been experimentally confirmed that the zwitterionic TPPS<sub>4</sub> aggregates spectroscopically feature absorption bands of J-aggregates at low pH value (the intermolecular electrostatic repulsion being weakened among the molecules due to the acidic medium) specifically in the B-band (400–500 nm) region.<sup>15</sup>

Tubular and striplike structures of TPPS<sub>4</sub> aggregates have been suggested, assuming that the zwitterionic TPPS<sub>4</sub> molecules self-assemble into a bent thread that can contain approximately 60–70 monomers in a loop.<sup>12,16</sup> The structures on silicon substrates were analysed with atomic force microscopy (AFM). It was determined that the size of the separate stripes varies from 4.5 nm × 40 nm × 200 nm to 4.5 nm × 40 nm × 1000 nm (height × width × length).<sup>12</sup>

Pleckaitis *et al.* published two possible structural models of TPPS<sub>4</sub> molecular nanotubes. In a face-exposed structure, TPPS<sub>4</sub> molecules have “adjacent” sulfonate (SO<sub>3</sub><sup>-</sup>) groups and these molecules oriented with the planar side towards the porphyrin nanotube surface, whereas in an edge-exposed structure, molecules have “opposite” SO<sub>3</sub><sup>-</sup> groups and these

molecules are put together with the edge exposed to the TPPS<sub>4</sub> nanotube surface.<sup>17</sup>

However, such microscopic-level information is not available in experiments. Additionally, only small molecular systems, mainly dimers, can be modeled with sufficient accuracy to describe ground and excited states by *ab initio* quantum chemistry methods, *e.g.* density functional theory (DFT).<sup>18–20</sup> Ishii *et al.* used DFT with Becke's three-parameter hybrid functional applying the non-local correlation provided by the Lee, Yang, and Parr (B3LYP) method along with the Pople 6-31G\* basis set for modelling similar types of H<sub>4</sub>TPPS<sub>1</sub> J-dimers. Right-handed helical, left-handed helical, or parallel structures have been found.<sup>20</sup> In our previous study, 5 different monomers and 10 dimers of TPPS<sub>4</sub>, differing by protonation pattern, were determined using DFT with the Coulomb-attenuating B3LYP functional (CAM-B3LYP) and Pople 6-31G(d,p) basis set. The influence of water (solvent) was also approximately evaluated with the polarizable continuum model (PCM). It has been shown that the dimers are dominant at pH 1.0, while the monomeric forms dominate at pH 12.1 to 3.0 and at pH –1.0. However, the calculations showed that zwitterionic TPPS<sub>4</sub> molecules and their dimers do not show curvature (or bending) and the proposed tubular aggregation remains inconsistent with the DFT-implied planar type of TPPS<sub>4</sub> molecular structure.<sup>21</sup>

Larger molecular aggregates may be necessary to address in order to expose the structural bending, influence of water molecules and thermal effects, which might demonstrate the accumulation effect. The classical molecular dynamics (MD) approach, based on classical equations of motion and using effective molecular mechanics (MM) intermolecular interactions, could be used for this purpose due to lower computational cost in comparison to quantum chemistry. MD simulations allow for finite temperature dynamical corrections due to the anharmonicity of interaction potentials. MD simulations provide a toolkit to study static and dynamical processes in larger systems consisting of tens of thousands of atoms.<sup>22,23</sup>

In a previous study, the chiral self-organization of diacid TPPS<sub>4</sub> (H<sub>4</sub>TPPS<sub>4</sub><sup>2-</sup>) tetramers was theoretically simulated. Despite the progress of porphyrin chiral self-organization investigations,<sup>24</sup> very little is known about the zwitterionic TPPS<sub>4</sub> (H<sub>6</sub>TPPS<sub>4</sub><sup>0</sup>) form aggregation. In this study, starting from quantum mechanical (QM) calculation of H<sub>6</sub>TPPS<sub>4</sub><sup>0</sup> monomers Z1 and Z2 (see Fig. 2(a–c) inside the blue rectangles), the molecular structures were parametrized for MM optimization and MD simulations leading to an updated force field (FF). A fluctuating exciton model based on the MD trajectory was constructed. Linear absorption and circular dichroism (CD) spectra, which are very sensitive to the molecular organization,<sup>25,26</sup> were calculated for the obtained chiral tetramers. Correlation between the modelled and the experimentally measured<sup>21</sup> spectra was used to suggest the favourable aggregation type of the TPPS<sub>4</sub> aggregates.



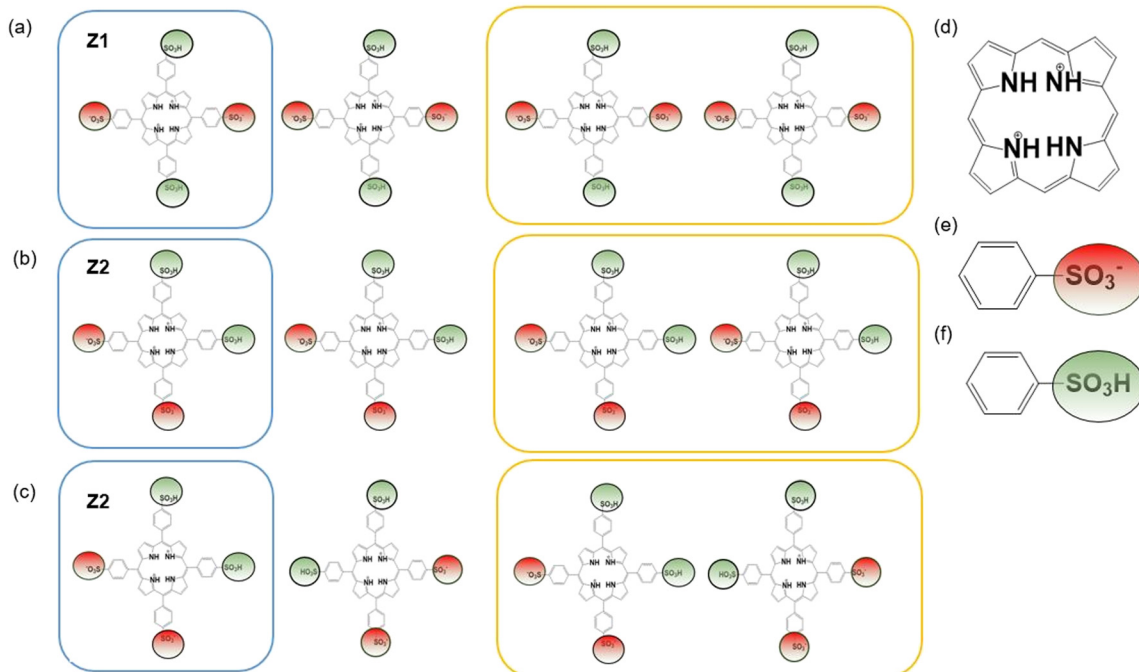


**Fig. 2** Chemical structure of the  $\text{H}_6\text{TPPS}_4^0$  monomers (inside blue rectangles) and dimers (inside orange rectangles) constructed from this monomer. Tetramers are obtained by all four monomers in a row. (a) Z1 – zwitterionic form aggregates, where  $\text{SO}_3\text{H}$  groups are opposite, (b) Z2 – zwitterionic form aggregates, where  $\text{SO}_3\text{H}$  groups are adjacent, (c) other form of Z2 aggregation. Charged parts of the molecule: (d) positively charged porphyrin ring (charge +2), (e) charged sulfonatophenyl group ( $\text{SO}_3^-$  – red), (f) neutral sulfonatophenyl group (protonated  $\text{SO}_3\text{H}$  – green). Z1 tetramer in (a) and Z2 tetramer in (b) are possible structures to form extended aggregates, Z2 tetramer in (c) cannot grow because of electrostatic interactions.

## Results and discussion

The QM optimized  $\text{TPPS}_4$  structures of Z1 and Z2 monomers are shown in Fig. 3(a) and (b), respectively. As these forms of the porphyrin molecule are charge-neutral, we have shown by quantum mechanical calculations that they tend to form dimers.<sup>21</sup>

These structures are very similar to those used in our previous publication.<sup>21</sup> However, in the present study, we obtained the Z1 and Z2 monomers using B3LYP with the Pople 6-311G(d,p) basis set, whereas in ref. 21, we used CAM-B3LYP with the Pople 6-31G(d,p) basis set. In this study, the

B3LYP method was used because we calculated separate molecules (monomers) and in this case long-range Coulomb interaction is not important. Therefore, these structures are not equivalent. B3LYP calculations were not used for larger structures. Here we point out that the Z1 monomer has almost perfect  $C_2$  symmetry, unlike Z2. Additionally, the side rings (of benzene) are much more twisted in Z2. Apparently, the symmetry of the molecule significantly affects the electron distribution in the porphyrin ring, which affects the twisting of the side rings. These structures and their mechanical properties are used to parameterize classical force fields specifically for these molecules.

The MM optimized geometries of the  $\text{TPPS}_4$  Z1 and Z2 monomers with the numbers of carbon and nitrogen atoms used in this paper are presented in Fig. 4(a) and (b), respectively.

It was observed that phenyl groups with non-protonated sulfonate groups ( $\text{SO}_3^-$ ) in *para* positions are more twisted than phenyl groups with protonated sulfonate groups ( $\text{SO}_3\text{H}$ ) in *para* positions in both the Z1 and Z2 monomers (Fig. 4(a) and (b)). Atom types of these monomers were assigned automatically with the Antechamber program<sup>27</sup> and revised upon visual inspection. The overlap of the  $\text{TPPS}_4$  Z1 and Z2 monomer structures optimized with B3LYP/6-311G(d,p) and MM optimized structures with marked atom types, which were changed, are depicted in Fig. 4(c) and (d), respectively. Other atom types were not

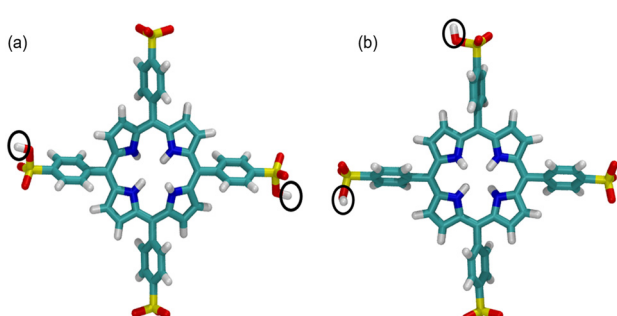


**Fig. 3** QM optimized structures of  $\text{TPPS}_4$  monomers. (a) Z1 monomer, (b) Z2 monomer. Hydrogens of  $\text{SO}_3\text{H}$  groups are surrounded by a black oval.



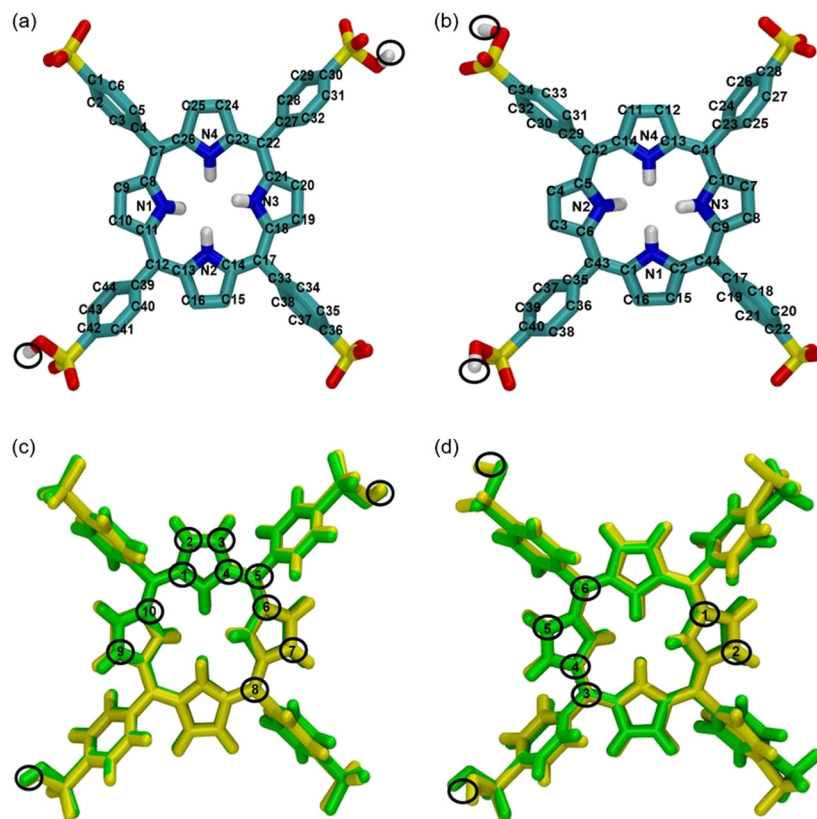


**Fig. 4** MM optimized structures of  $\text{TPPS}_4$  monomers and overlap of the  $\text{TPPS}_4$  monomer structures optimized with DFT B3LYP/6-311G(d,p) (green) vs. MM (yellow).  $\text{TPPS}_4$  monomers with the numbers of carbon and nitrogen atoms: (a) Z1 monomer, (b) Z2 monomer, (c) QM and MM optimized Z1 monomers, (d) QM and MM optimized Z2 monomers. New atom types at MM level: 1;2;6;9 - "cc"; 3;4;7;10 - "cd"; 5;8 - "ce" (Z1 monomer) and 1;5 - "cd"; 2;4 - "cc"; 3;6 - "ce" (Z2 monomer). (a) and (b) Hydrogen atoms are not shown except the ones bonded to oxygen and nitrogen atoms; (a)-(d) hydrogens of  $\text{SO}_3\text{H}$  groups are surrounded by a black oval.

changed. Technical information on MM optimized Z1 and Z2 monomers is presented in the ESI.<sup>†</sup>

A comparison of parameters (bond lengths, valence angles and dihedral angles) between  $\text{TPPS}_4$  Z1 and Z2 monomer structures optimized with QM vs. MM is presented in Tables 1–3. Table 1 presents only bonds with lengths that differ the most between QM and MM structures, *i.e.* absolute length difference equal to 0.02 Å.

This shows that the reparameterization resulted in very good FF representation (note that the difference in bond

**Table 1** Bond lengths (Å) of Z1 and Z2 monomers after QM and MM optimization

Bond lengths (Å)	Z1 monomer	
	QM	MM
C23–C22	1.40	1.42
C13–C12	1.40	1.42
Z2 monomer		
QM	MM	
N1–C1	1.38	1.40
C6–C43	1.40	1.42
C5–C42	1.40	1.42

lengths in the other tetrapyrrole (pheophytin *a*) structure is up to 0.15 Å between QM and MM structures in a previous study<sup>28</sup>.

The valence and dihedral angles of  $\text{TPPS}_4$  monomer macrocycles (see Tables 2 and 3) were also compared between QM and MM structures. It was noticed that the largest differences are 3.38° (Z2 monomer, C2–C44–C9), 13.27° (Z1 monomer, C14–C17–C33–C34) and 15.83° (Z2 monomer, C2–

**Table 2** Valence angles of Z1 and Z2 monomers after QM and MM optimization

Valence angles (°)	Z1 monomer	
	QM	MM
C26–C7–C8	126.47	129.33
C23–C22–C21	125.42	125.08
C14–C17–C18	126.46	129.37
C11–C12–C13	125.42	126.08
Z2 monomer		
QM	MM	
C5–C42–C14	125.54	127.07
C10–C41–C13	126.47	127.38
C1–C43–C6	127.15	127.38
C2–C44–C9	124.66	128.04



**Table 3** Dihedral angles of Z1 and Z2 monomers after QM and MM optimization

Dihedral angles (°)	Z1 monomer	
	QM	MM
C13–C12–C39–C44	–120.67	–123.88
C14–C17–C33–C34	–117.12	–103.85
C26–C7–C4–C3	117.19	107.67
C23–C22–C27–C32	120.64	122.00
Z2 monomer		
	QM	MM
	–109.99	–121.44
C1–C43–C35–C37	–125.61	–109.78
C2–C44–C17–C18	118.59	118.59
C13–C41–C23–C25	118.11	110.65

C44–C17–C18). Hence, structures of the Z2 monomer with “adjacent”  $\text{SO}_3\text{H}$  groups differ more than those of the Z1 monomer with “opposite”  $\text{SO}_3\text{H}$  groups at QM and MM level.

Conversely, in the pheophytin  $\alpha$  structure,<sup>28</sup> the largest valence angle difference is equal to  $8.3^\circ$  (larger than in our structures).

Despite the fact that the MM Z2 monomer (Fig. 4b) is deformed compared to the QM Z2 monomer (Fig. 3b), as shown in Fig. 4(c) and (d), the QM and MM optimized structures of our monomers (including both Z1 and Z2) are very similar. The tetramers were constructed gradually to keep the simulation stable as described in section Computational details. 100 ns MD simulation was performed for solvated tetramers.

In order to know whether  $\text{TPPS}_4$  Z1 and Z2 tetramers form some type of curved structure, the Z1 and Z2 tetramer global structures were inspected by introducing an intermolecular curvature angle, which is recorded along the MD trajectory (see Fig. 5(c) and (d), respectively). The molecules were numbered 1 to 4 in a row. A first vector,  $\vec{a}_{12}$ , is drawn between the porphyrin ring centres of the first and second  $\text{TPPS}_4$  (these are mass centres defined by the corresponding

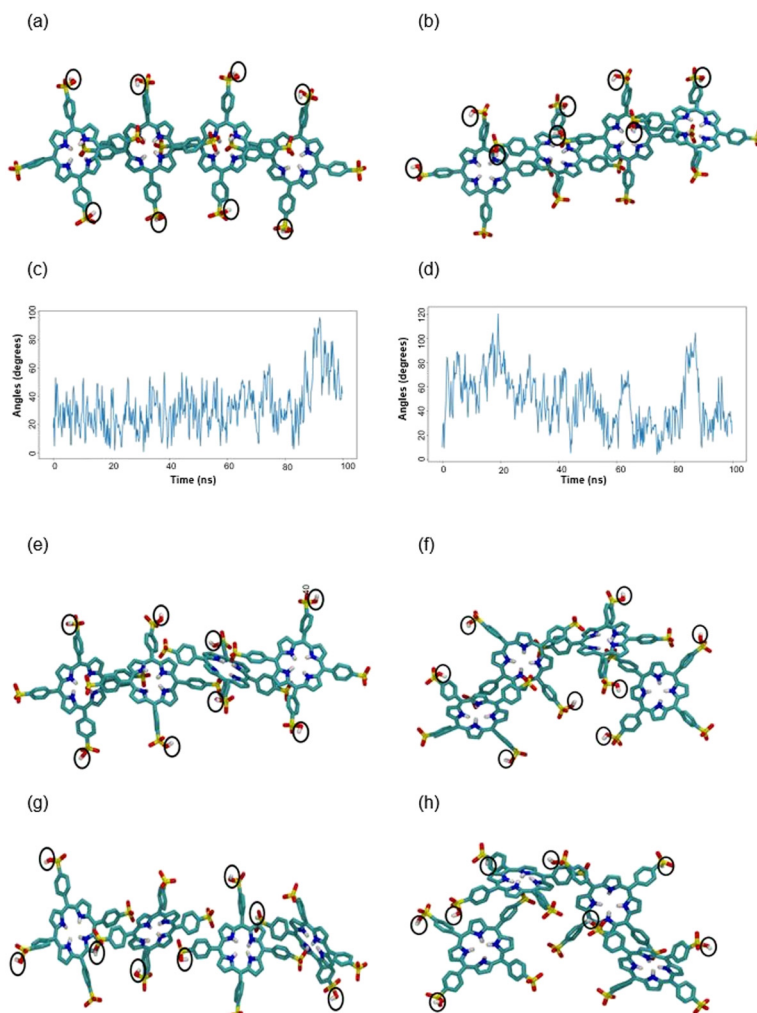


**Fig. 5** (a and b) Initial structures of  $\text{TPPS}_4$  (a) Z1 and (b) Z2 tetramers. (c and d) The curvature angle  $\alpha$  variation along the trajectory for (c) Z1 and (d) Z2 tetramers. (e) Z1 tetramer when  $\alpha$  angle is smallest and (f) when  $\alpha$  angle is largest. (g) Z2 tetramer when  $\alpha$  angle is smallest and (h) when  $\alpha$  angle is largest. Hydrogen atoms are not shown except the ones bonded to oxygen and nitrogen atoms. Hydrogen atoms of  $\text{SO}_3\text{H}$  groups are marked by a black oval.



four nitrogen atoms of the four molecules). A second vector,  $\vec{a}_{34}$ , is drawn between the porphyrin rings of the third and fourth  $\text{TPPS}_4$  molecules. Then the angle between these two vectors (by using the dot product definition) is given by:

$$\alpha = \arccos \frac{\vec{a}_{12} \cdot \vec{a}_{34}}{|\vec{a}_{12}| \cdot |\vec{a}_{34}|}, \quad (1)$$

This angle is zero when the tetramer is linear (I-like shape), or the tetramer forms a N-like shape. These two shapes do not show a global curvature. However, the angle is always a positive number between  $0^\circ$  and  $180^\circ$  when the tetramer's structure is of C-like shape, *i.e.* when there is a global curvature. The importance of this approach is that it excludes information on simple structure rotation, which is not relevant for our analysis.

The results, reported in Fig. 5(c) and (d) show that the molecules form a curved structure having permanent curve angle  $\alpha = \sim 30^\circ$ . Structures with the smallest/largest  $\alpha$  are depicted in Fig. 5(e) and (f) for the Z1 tetramer, and in Fig. 5(g) and (h) for the Z2 tetramer. The largest curvature for Z1 ( $\alpha = 96^\circ$ ) is found at 92 ns, while in Z2 a larger maximum angle ( $\alpha = 121^\circ$ ) is found at around 19.2 ns. It is also noticed that in the Z2 tetramer after simulation (Fig. 5(g)), the second and fourth  $\text{TPPS}_4$  residues were rotated by  $\sim 270^\circ$  compared with the initial Z2 tetramer (Fig. 5(b)). Hence, our results show that  $\text{TPPS}_4$  forms a curved structure. Meanwhile, El-Hachemi *et al.*<sup>29</sup> determined by X-ray and electron diffraction methods that  $\text{H}_4\text{TPPS}_4^{-2}$  forms sheets along the [101] plane direction. According to their results, each porphyrin molecule is slightly rotated. Moreover, the porphyrin macrocycle is almost perpendicular to this plane. It causes a decrease in the symmetry in the structure on the plane mentioned above. Due to these reasons, parallel dimers are arranged as  $\pi$ -stacks. However, we cannot compare these results directly because we use different protonation patterns of  $\text{TPPS}_4$  (our porphyrin is electrically neutral, while the authors investigated the diacid form). Moreover, these authors investigated the crystal architecture of  $\text{TPPS}_4$ , while we simulated  $\text{TPPS}_4$  tetramers solvated with a water box.

In order to qualitatively assess whether this permanently curved and fluctuating structure is feasible, we performed absorption spectra calculation using the Frenkel exciton model, which has been successfully used for calculating absorption and CD.<sup>30</sup>

Due to its structural symmetry,  $\text{TPPS}_4$  has two degenerate optical transitions for each absorption band. Two absorption bands are mostly considered for this type of molecules,<sup>21</sup> thus leading to four transitions per molecule.

The  $\text{TPPS}_4$  molecule would have  $C_4$  symmetry if hydrogen atoms were ignored. Only the electrons of the porphyrin ring are optically active. Hence, the protonation state of distant  $\text{SO}_3$  groups should not affect significantly the optical transitions. For such symmetry all electronic excitations are doubly degenerate with perpendicular, *e.g.*  $x$  and  $y$ , transition dipoles in the symmetry plane. The exact orientation of these dipoles is irrelevant, because for degenerate transformation

the two quantum basis states could be used to construct equivalent “twisted” basis functions as their two linear superpositions. The two basic transitions can be conveniently placed along the four nitrogen atoms.

However, the Z1 and Z2 forms of the  $\text{TPPS}_4$  molecule have reduced symmetry since, during the MD run, the molecular geometry fluctuates. Thus, an arbitrary transition dipole placement does not hold, so we have considered two models for dipole configurations. Consider a single molecule. Considering two absorption bands (Q and B), two transitions per single absorption band, there are four transitions per molecule with four transition dipoles. The two dipoles of the Q band are perpendicular, while the other two dipoles of the B band are also perpendicular, and the orientation of the Q dipole with respect to the B dipole is not defined. Perpendicular transition dipoles can be placed along lines connecting opposite nitrogen atoms (giving two perpendicular directions). Additionally, we can consider directions which are diagonal to the lines connecting the nitrogen molecules. Consequently, for the two absorption bands we can consider two models for transition dipole orientations, as shown in Fig. 6: two of them are perpendicular to the other two. In both models the transition dipoles of the Q band are perpendicular, and the transition dipoles of the B band are perpendicular. However, in model I transition dipoles of the B band make a  $45^\circ$  angle with transition dipoles of the Q band, while in model II transition dipoles of the B band have the same directions as transition dipoles of the Q band. As the molecules fluctuate along the trajectory, the transition dipole orientations (and angles between them) slightly fluctuate, making these two models not equivalent.

The given set of dipole vectors of a single molecule (model I and model II) are used for all four molecules in the tetramers. Note that all parameters except the molecular transition energies and transition dipole amplitudes are fluctuating along the MD trajectory. Consequently, the resonant couplings fluctuate along with the transition dipole orientations and intermolecular distance fluctuations.

The calculated absorption and CD spectra are averaged along the MD trajectory. For reference, in Fig. 7 and

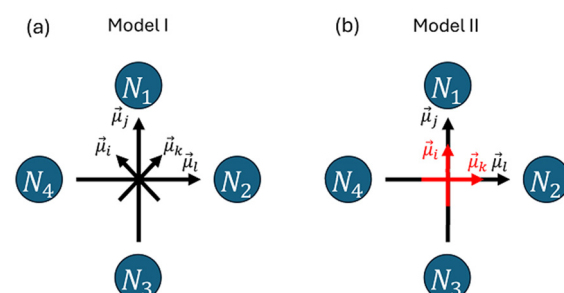


**Fig. 6** Models (a)-I and (b)-II of optical transition dipole orientations in relation with the  $\text{TPPS}_4$  molecule's nitrogen atoms, with  $\vec{\mu}_i$  and  $\vec{\mu}_k$  corresponding to the optical transition energies of the Q band and  $\vec{\mu}_j$  and  $\vec{\mu}_l$  for the B band.



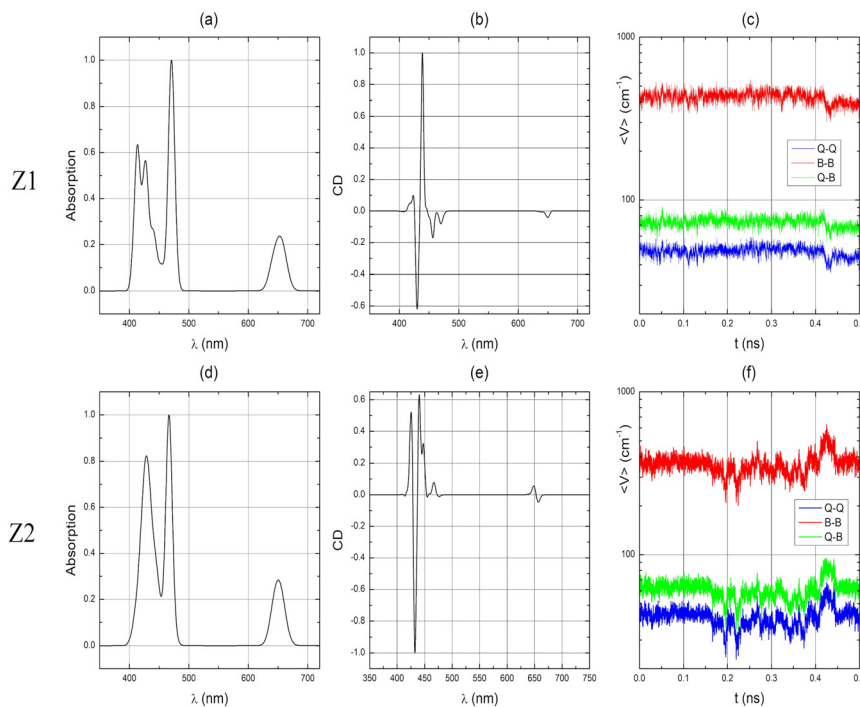


**Fig. 7** Calculated absorption (a and d) and CD spectra (b and e) and dynamics of the average strength of the intermolecular couplings of the Q-Q, B-B and mixed Q-B bands (c and f) of model I dipole configuration of the Z1 and Z2 tetramers. For definitions of the models see sec. Computational details.

8(c and f) we present the calculated nearest-neighbour coupling constants, averaged across the Hamiltonian matrix

for the same kind of interactions: we thus have three types: Q-Q, mixed Q-B and B-B couplings. It can be observed that

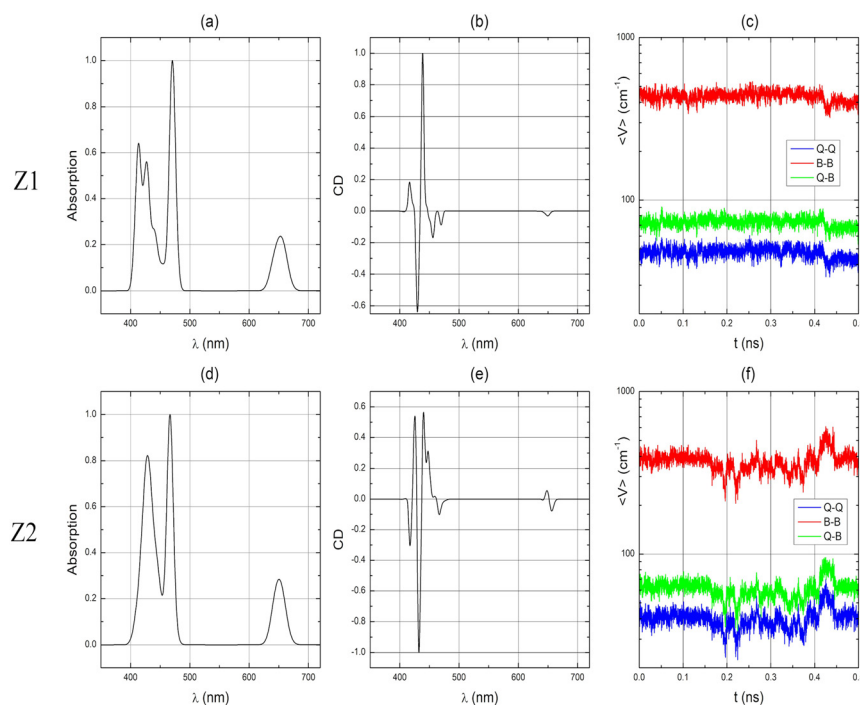


**Fig. 8** Calculated absorption (a and d) and CD spectra (b and e) and dynamics of the average strength of the intermolecular couplings of the Q-Q, B-B and mixed Q-B bands (c and f) of model II dipole configuration of the Z1 and Z2 tetramers. For definitions of the models see sec. Computational details.

average values can be established for Z1 monomers and relative fluctuations for all types of couplings are the same. Z2 monomers show a slightly larger variation of the couplings. The dynamics of the average strength of the intermolecular couplings of the Q-Q, B-B and mixed Q-B bands in Fig. 7 and 8(c and f) correlate with the change in both the Z1 and Z2 tetramer's curvature  $\alpha$  angles (Fig. 5c and d).

Absorption and CD spectra for both Z1 and Z2 tetramers, for two dipole models (in Fig. 6), are shown in Fig. 7 and 8(a, b, d and e) and are summarized in Table 4. Both models show almost identical absorption with splitting of the B band with a strong peak at  $\sim 470$  nm. Another peak is at 428 nm for the Z2 type tetramer, while this feature further splits in the Z1 tetramer. The molecular transition is at 435 nm (see model parameters below, eqn (2)). The 470 nm band in the spectra is often denoted as the J band, while the 425 nm feature is the H band.

The Q band has a much simpler profile (the fine sub-peaks are not resolved with the given linewidth) showing a single peak at  $\sim 650$  nm which is red-shifted from molecular transition at 646 nm (see model parameters below, eqn (2)). Most notably, there is a difference between Z1 and Z2 tetramers in absorption only in the B band region.

CD spectra are much more sensitive to fine structure fluctuations, which is confirmed by the calculated result: fine variations of the spectral line incomplete convergence with respect to fluctuations; however, the spectral variations are small and the trend is clear. The Z1 tetramer in B band demonstrates a  $- +$  pattern for model I and a  $+ - +$  pattern for model II (from blue to red spectral region). Only a negative feature is observed for both models in the Q band. The Z2 tetramer demonstrates a  $+ - +$  pattern for model I dipole configuration and a  $- + -$  pattern for model II dipole configuration in the B region, whereas this tetramer demonstrates a  $+ -$  obvious pattern for both models in the Q band. The crossing points of the zero amplitude line are listed in Table 4.

TPPS<sub>4</sub> molecules in acidic conditions are known to self-organize into extended cylindrical structures as confirmed by experiments. In our previous study we used quantum mechanical optimization of molecular dimers to sort out possible structures which are stable and can grow into larger structures. However, the quantum mechanical optimization

can hardly be extended to large structures. As a result, here we switch to classical molecular dynamics.

Using MD simulations, we seek to reveal the main molecular building blocks which lead to formation of the structures. MD relies on classical force fields, which are parameterized for specific molecular bonding and intermolecular interactions. The force field has been extensively parameterized for molecular short-range properties (bond lengths, valence angles, ...).<sup>28,31</sup> However, optically active molecular chromophores usually contain extended conjugated structures, which have unique electronic configurations. Accordingly, the force field has to be adjusted for the given chromophores.

TPPS<sub>4</sub> molecules possess intricate cyclic structures. Structurally, a porphyrin molecule comprises four pyrrole rings. Each of these rings contains one nitrogen and four carbon atoms connected by  $-\text{CH}=\text{}$  linkages. The center of the porphyrin ring in TPPS<sub>4</sub> binds protons. Symmetric configuration of bonds leads to formation of cyclic 18  $\pi$ -electron ring system, which connects the four pyrrole rings and their linkers. According to our calculations, direct application of general Amber force field (GAFF) leads to a molecular structure which significantly deviates from the quantum chemistry optimized result. Hence, reparametrization has been performed. Molecular geometry optimization using classical force fields leads to an almost perfect match of the molecular optimal geometry.

Linear Z1 and Z2 tetramers were constructed and the tetramer structures were optimized in an explicit water box. This leads to a specific structure; however, the structure cannot be understood as necessarily the most optimal. It is merely one possibility because at room temperature the solvent has sufficient thermal energy to shift the molecule out of the potential minimum and a variable structure becomes a better representative of the typical structure.

A global structure parameter becomes necessary to introduce for fluctuating structure characterization. Schifino *et al.* used a tilting angle between TPPS<sub>4</sub> porphyrin rings.<sup>24</sup> We thus use a similar parameter – the curvature  $\alpha$  angle; however, it covers more extended geometrical information. The tilting angle in Schifino *et al.*'s study of Rac-H<sub>4</sub>TPPS<sub>4</sub><sup>2-</sup> tetramer varies more than our  $\alpha$  angle (and structures) of Z1 and Z2 tetramers. However, we cannot compare these results

**Table 4** Main peaks of theoretically calculated absorption spectra and 0 intensity intercepts of calculated CD spectra for each model. Due to fluctuations, the intercept points should be considered only approximately

Absorption spectra			CD spectra		
Model <sup>a</sup>	Tetramer	B (nm)	Q (nm)	B (nm)	Q (nm)
I	Z1	413, 428, 440, <b>470<sup>b</sup></b>	652	425, 434, 448	— <sup>c</sup>
	Z2	428, <b>466<sup>b</sup></b>	650	428, 437, 475, 480	653
II	Z1	413, 428, 440, <b>470<sup>b</sup></b>	652	425, 434, 448	— <sup>c</sup>
	Z2	428, <b>466<sup>b</sup></b>	650	421, 428, 437, 461	652

<sup>a</sup> Model by orientation of the optical transition dipole vectors (see Fig. 6). <sup>b</sup> Boldface denotes the strongest spectral peaks. <sup>c</sup> “—” denotes a spectral peak with no intersect with  $y = 0$ .



directly because we performed plain molecular dynamics simulations, while Schifino *et al.* performed enhanced sampling simulations with parallel bias metadynamics.<sup>24</sup> Moreover, our structures have a different protonation pattern (our chromophore is electrically neutral). Their main result is that axial chirality affects the chiral self-assembly of the H<sub>4</sub>-TPPS<sub>4</sub><sup>2-</sup> porphyrin in larger supramolecular structures. On the other hand, our Z1 and Z2 tetramers are “racemic”, *i.e.* they have 2 positive and 2 negative dihedral angles and one tetramer, which as determined by the above-mentioned authors is also racemic.

Our previous calculations based on dimers did not reveal any tilt between neighbouring molecules. We thus find that larger molecular structures in explicit water are necessary to reveal structural curvature. The important result here is that such curvature remains conserved at room temperature in the presence of extensive fluctuations. Such formation hence could be behind the formation of cylindrical structures when the number of molecules increases. As was mentioned above, TPPS<sub>4</sub> tetramers form structures with a permanent curve angle ( $\alpha$ ) of approximately 30°. Longer aggregates would tend to curve into a ring. A full ring of the nanotube structure spans 360°. Therefore, if four molecules correspond to ~30°, then 48 molecules will correspond to 360°, indicating that the nanotube ring should contain approximately 48 TPPS<sub>4</sub> molecules. This result aligns well with literature data, which suggest that aggregates typically contain 60–70 monomers in a ring, as determined by comparing experimentally measured and theoretically calculated results.<sup>12,16</sup> However, at least two-dimensional larger structures may be necessary to characterize.

The most direct correlation to experiment can be performed by considering spectra of molecular structures. Indeed the spectroscopic properties significantly depend on intermolecular resonant interactions. This forms the basis of the Frenkel exciton model, which assumes different molecules interacting only electrostatically and electron exchange is not included. The model allows calculating the spectra with such restrictions, which usually yield sufficiently accurate results.

Using MD variation of the structure yields variation of the spectra. The trajectory thus has to be sufficiently long so that the calculated spectra cover the most probable structure variations and shows the converged result. We have checked the convergence of the spectra by inspecting the variation of the spectra with the number of frames included. In Fig. 9 we show that the number of frames included in our calculations only slightly affects the intensity of the spectral peaks in the B band (the Q band remains constant). We can see in Fig. 10 that the number of frames that we use in our theoretically calculations only slightly changes the intensity of the B band in the CD spectrum as well. This confirmation of CD is very important as the CD spectrum is very tightly related to molecular structure variations as it is directly induced by structural chirality. As independent molecules in the dipole approximation are assumed to be non-chiral, the CD

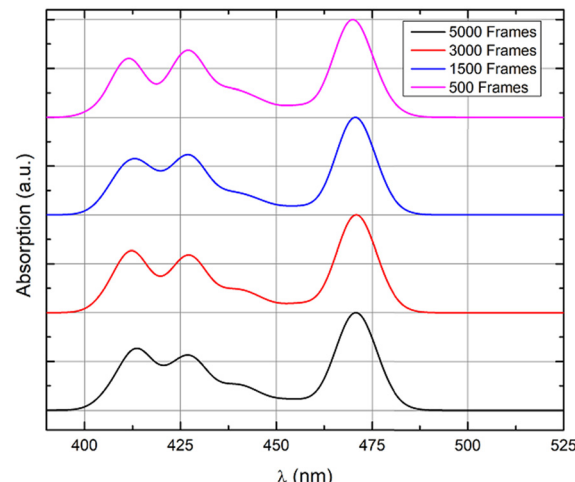


Fig. 9 Calculated B band of the Z1 tetramer of model I averaged over different numbers of frames. For definitions of the models, see Fig. 6.

spectrum becomes induced by global properties of the tetramer. Hence, the CD spectrum directly indicates the effect of the chiral curvature of the structure.

One of the targets is related to defining the most probable zwitterionic structure by comparing to experimental data. In our previous study, we determined that the theoretically calculated results for the monomers and dimers support the experimentally observed spectral shift when the pH values decrease from pH 7.1 to pH 1.0 (ref. 21) (on the other hand, the spectral shift obtained by quantum chemical methods does not coincide with experimentally measured data when the pH decreases from 1.0 to -1.0). Our previous studies revealed that the J<sub>3</sub><sup>(0)</sup> dimer (which forms from the Z2 monomer) is the most likely initial structure to form larger structures at pH 1 (ref. 21) (see corresponding dimer scheme in Fig. 2(b) inside the orange rectangle). In our present calculations in Fig. 5(c and d) we find that the Z1 tetramers

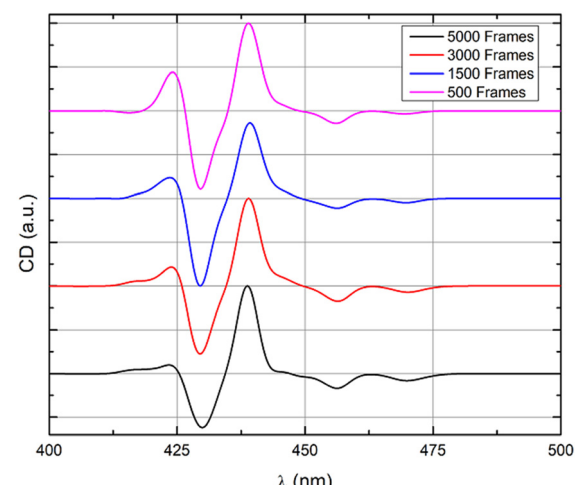


Fig. 10 Calculated B band CD spectra of the Z1 aggregate of model I averaged over different numbers of frames. For definitions of the models, see Fig. 6.



are slightly more compact than Z2 – the variation of the curvature angle of the Z1 tetramer is smaller and the angle itself is smaller, hence the Z2 tetramer is more curved. As the result the intermolecular interactions (e.g. B–B type in Fig. 7(c and f)) in the Z2 tetramer are slightly smaller compared to that in the Z1 tetramer. The difference in interactions results in a slightly distinct B band between the Z1 and the Z2 tetramers: the B band of the Z1 tetramer shows four distinct peaks (with the strongest peak at 470 nm), while only two peaks are resolved in the case of the Z2 tetramer. Our present calculations of absorption spectra of Z1 and Z2 tetramers, corresponding to pH 1.0, show that the peaks in the B and Q regions become red-shifted (Table 4) compared to that of the monomers (Table 1 (ref. 21)). These results very well coincide with literature data.<sup>14</sup> Eventually, the difference between absorption of Z1 and Z2 tetramers is quite small; however, the larger red-shift of the Z1 tetramer better represents the experiment, where the aggregate-related peak (B band) was identified at 490 nm. This does not rule out the significance of the Z2 form. However, more research on this topic needs to be undertaken in order to know whether Z1 or Z2 TPPS<sub>4</sub> forms are more probable candidates to form large aggregates, or whether mixed Z1–Z2 aggregation is also possible.

In many of the spectra of J-aggregated TPPS<sub>4</sub> porphyrins reported so far in the literature (see *e.g.* ref. 32 and 33), the spectral features at 490–492 nm are rather sharp and are often used as aggregate markers. The aggregate-related peak in ref. 21 is broad and relatively small. We can easily show that this broad linewidth is related to variation of the intermolecular couplings or to different levels of aggregation. As an example, we have used our MD trajectory and calculated spectra including only dimers and trimers by neglecting other chromophores. We can see that when we decrease the number of molecules in our model, the gap between the most pronounced peaks of the B band decreases and becomes closer to the shape expected in a monomer. Even when considering a dimer, the splitting of the B band is still very pronounced (Fig. 11). If the large J-aggregates have a peak at 490 nm, the smaller ones should be somewhat more blue-shifted. However, from Fig. 11, the tetramer already shows a significantly red-shifted band compared with monomers (and dimers). As such, it may be that the majority of the red shift is already present at the level of the tetramer. We also note that the spectra of ref. 21 were done at small concentrations. Spectroscopic characteristics and changes with respect to the number of molecules (Fig. 11) are the same for Z1 and Z2.

The most sensitive spectroscopic structure probable is the CD spectrum. The CD spectra are difficult to compare to experimental results as the TPPS<sub>4</sub> tetramers may exist only at very low concentrations, too low for quality CD measurements. Hence, we did not find quality experimental CD spectra of TPPS<sub>4</sub> at very low concentrations. Additionally, the CD spectra are dependent not only on the solute but also on the solution environment, and induced dichroism is often obtained,<sup>34,35</sup> which has been observed for TPPS<sub>4</sub>-type

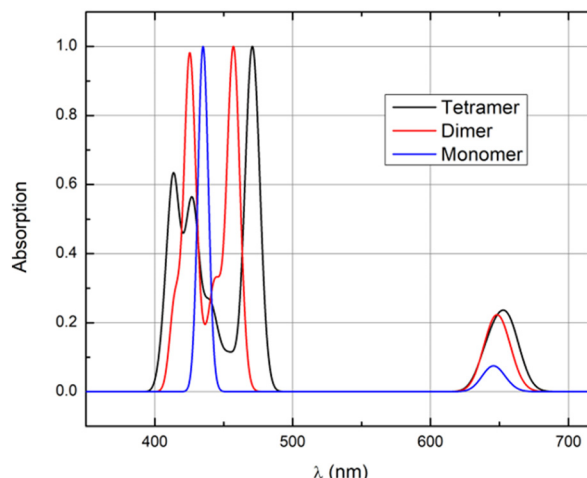


Fig. 11 Calculated absorption spectra of a monomer, dimer and tetramer of Z1 aggregate model I. For definitions of the models, see Fig. 6.

J-aggregates when the pH of the solution is about 1.<sup>36</sup> On the other hand, this does not mean that J-aggregates under these conditions are not chiral. Most probably the solution involves racemic mixtures of chiral aggregate molecules and their CD signals compensate for each other. For this reason, the calculated CD spectra are presented as the reference spectra, which can be used for future studies.

The racemization phenomenon of TPPS<sub>4</sub> was investigated experimentally by D'Urso *et al.*<sup>37</sup> They determined that the intensity and sign of the CD signal in H<sub>2</sub>TPPS<sub>4</sub><sup>-4</sup> and H<sub>4</sub>-TPPS<sub>4</sub><sup>-2</sup> spectra dynamically depend on mechanical stirring direction (clockwise and counterclockwise). Hence, the equilibrium of a racemic TPPS<sub>4</sub> mixture shifts by stirring. Moreover, the chirality also depends not only on mechanical stirring but also on the reagent mixing order, *i.e.*, whether porphyrin is added as the first or as the last reagent in the solution.<sup>38</sup> Furthermore, it was determined that counter-anions probably influence the precursor (initial dimer) formation and the stabilization of the oligomeric structures of TPPS<sub>4</sub>. The sign and intensity of the CD signal also depend on the hydrogen bonding ability of the various anions.<sup>39</sup>

It must also be taken into consideration that our Hamiltonian calculation approach is approximate – we include only dipole–dipole interactions. Higher-level intermolecular coupling calculation can be performed using the Poisson-TrEsp approach,<sup>40</sup> which has higher accuracy at small intermolecular distances, *i.e.* for nearest-neighbour molecules in the aggregates. Additionally, the description of the dielectric environment is improved by self-consistent solution of the Poisson equation, which may be relevant for our system since molecules have non-uniform charge distribution. However, these developments for TPPS<sub>4</sub> aggregates would be important for direct comparison with experiments, while here we present the qualitative estimations.

All in all, this study employs MD simulations for modelling molecular aggregation, which is a nontrivial



computation problem. MD simulations still lack reliability for extrapolating and predicting structures or processes. Our study is thus tightly correlated with experimental observations and therefore provides the missing molecular-level link towards formation of  $\text{TPPS}_4$  nanotubes. For this purpose, the highly symmetric metal-free porphyrin macrocycle was parametrized, *i.e.* GAFF parameters for  $\text{TPPS}_4$  were determined. A curvature angle  $\alpha$  was introduced for global structure characterization. Such analysis could help to analyse larger chromatophore ( $\text{TPPS}_4$  and similar) aggregates.

Regarding the reliability, the results were correlated with experimental observations: not only absorption and CD spectra but also dynamics of the average strength of the intermolecular couplings of the Q–Q, B–B and mixed Q–B bands improve the prediction of aggregate spectroscopic characteristics, which could be related with quantum energy wiring efficiency. Our complex approach to the problem of molecular cooperative quantum response is a solid step towards bottom-up approach molecular aggregation.

## Computational details

The zwitterionic form of  $\text{TPPS}_4$  ( $\text{H}_6\text{TPPS}_4^0$ ) dominates at a pH  $\approx 1$ .<sup>8,21,41</sup> There are two types of zwitterionic monomers: the “opposite” zwitterion, where  $\text{SO}_3\text{H}$  groups are opposite (which we denote as Z1, as we did in our previous article<sup>21</sup>), and the “adjacent” zwitterion, where  $\text{SO}_3\text{H}$  groups are adjacent (denoted as Z2 (ref. 21)). The initial  $\text{TPPS}_4$  structures were constructed by hand using the GaussView 6.1 software package.<sup>42</sup> *Ab initio* QM geometry optimization of the zwitterionic  $\text{TPPS}_4$  Z1 and Z2 monomers (see Fig. 2(a–c) inside blue rectangles) was performed to determine the molecular configuration using the DFT B3LYP method along with the Pople 6-311G(d,p) basis set. The polarizable continuum model (PCM) was used to evaluate the influence of water (solvent).<sup>43</sup> All QM calculations were performed using the Gaussian 16 software package.<sup>44</sup>

The MM and MD methods are based on optimized inter-atom interaction potentials, commonly referred to as an atomic force field. Classical FF, including one of the most widespread GAFF, characterizes two types of interactions: chemically bonded and non-bonded. Parameters of bonded interactions characterize bond lengths, bond angles, and dihedrals (torsional) angles. Hence, covalent bond stretching and valence angle bending are parameterized using the harmonic models, while a harmonic function is used for dihedral twisting energy. The non-bonded interactions are characterized by electrostatic and van der Waals terms.<sup>45,46</sup>

GAFF has parameters for most organic molecules made of C, N, O, H, S, P, F, Cl, Br and I.<sup>47</sup> However, for some molecular systems, the parameters must be revised due to the extended conjugation of C=C bonds in pigments.<sup>48</sup> Since  $\text{TPPS}_4$  has a complex electron delocalization it is necessary to adjust the FF parameters. There is little published data about tetrapyrroles parametrization. To date, only naturally found tetrapyrrole-like pigments have been parametrized for MM:

Guerra *et al.* performed chlorophyll *a* and pheophytin *a* FF parametrization,<sup>28</sup> while Zhang *et al.* developed new FF parameters for metalloporphyrin heme *b*.<sup>31</sup> However, these parameters do not apply to  $\text{TPPS}_4$  since chlorophylls have different macrocycles and symmetry. There is no published FF for synthetic tetrapyrroles such as  $\text{TPPS}_4$ , which is structurally more symmetric than, *e.g.* chlorophylls (especially the Z1 form). In the present case several atom types, bond lengths, valence angles and dihedral angles were adjusted for bonded interactions for both Z1 and Z2 zwitterions. The obtained set of parameters is combined in the ESI.† Atomic partial charges of  $\text{TPPS}_4$  were derived by fitting the electrostatic potential (ESP) of the molecule using the restrained electrostatic potential (RESP) model.<sup>47,48</sup> All parametrization and MM calculations were performed with AMBER 22 software package.<sup>49</sup>

Next, the dimers (see Fig. 2(a–c) inside orange rectangles, respectively) were constructed from  $\text{TPPS}_4$  Z1 or Z2 monomers (see Fig. 2(a–c) inside blue rectangles, respectively). Each dimer was solvated in a truncated octahedral box of water (one dimer in one box) with a 3-charge, 4-point rigid water model (OPC) with a distance of 10 Å between the solute and the edges of the box.<sup>50</sup>

The solvated structures were first optimized using 500 steps of steepest descent (SD) followed by 1500 steps of conjugate gradient (CG).  $\text{TPPS}_4$  aggregation experiments are usually performed at room temperature.<sup>3,51,52</sup> Due to this reason, after minimization, the molecular systems were heated to 298.15 K for 50 ps constant-volume, constant-temperature (NVT) ensemble simulations. Positional restraints (4 kcal mol<sup>-1</sup> Å<sup>-2</sup>) were applied to all non-hydrogen atoms of the  $\text{TPPS}_4$  dimers (and also tetramers). Next, a 1000 ps constant-pressure, constant-temperature (NPT) ensemble equilibration at 298.15 K was performed applying the same constraints on the structures. Finally, a production step of 100 ns at 298.15 K in the NPT ensemble was performed. A time step of 2 fs was used in combination with the SHAKE algorithm. Temperature and pressure were controlled with a Langevin thermostat and a Monte Carlo barostat as implemented in AMBER 22. Particle-mesh Ewald algorithm (PME) electrostatics with a short-range cutoff of 10 Å were used for all simulations.<sup>53</sup> Asymmetrical flat-bottom distance restraints were employed to limit the configurational space available to the tetramers. Specifically, these restraints were applied between the H(N) atoms of the porphyrin ring and the oxygen atoms of the sulphonate groups. The potential was left unchanged for distances below 9 Å to allow for a rearrangement of the tetramer structure while avoiding a complete dissociation of monomers (this was never observed for stable initial configurations).

The tetramers were constructed based on the structures extracted from dimer simulations (see Fig. 2(a) and (b)). Two linear Z1 and Z2 tetramers (see Fig. 5(a) and (b)) were constructed from the dimers and their MD simulation was performed. In the Z1 tetramer due to  $C_2$  symmetry, both negative sulfonate groups can be positioned to interact with



the positively charged porphyrin ring of its neighbour (see Fig. 5(a)), while in the Z2 tetramer only one negative sulfonate group can be interacting with the positively charged porphyrin ring (see Fig. 5(b)). The Z1 and Z2 tetramers were solvated in a truncated octahedral box of water before MD simulation. At least 12 Å were kept between the  $\text{TPPS}_4$  tetramers and the edges of the box. The simulation was run using the same conditions as for the dimers.

MD analysis was performed by using the CPPTRAJ<sup>54</sup> module of AmberTools. For trajectory visualization the Visual Molecular Dynamics (VMD) software was employed.<sup>55</sup> Typical obtained structures are shown in Fig. 5.

The two transitions are responsible for the Q band (600–700 nm), while the other two are related to the B (Soret) band (400–500 nm).<sup>56</sup> Consequently, the electronic Hamiltonian (unique for each MD frame) is given by

$$\hat{H} = \sum_{n=1}^N \sum_{i=1}^4 E_i |n_i\rangle\langle n_i| + \sum_{nm=1}^{n \neq m} \sum_{ij=1}^4 V_{ni,mj} |n_i\rangle\langle m_j|, \quad (2)$$

Here indices  $n$  and  $m$  mark different molecules,  $N = 4$  is the number of molecules,  $|n_i\rangle$  and  $|m_j\rangle$  are the states where the  $n$ th and  $m$ th molecules are excited to their  $i$ th and  $j$ th states, respectively, while other molecules remain in their ground states.  $E_i$  is the energy of state  $|n_i\rangle$ , while  $V_{ni,mj}$  is the resonant coupling constant between excitations  $|n_i\rangle$  and  $|m_j\rangle$ . The transition energies are assigned values of  $E_{1,2} = 15\,485 \text{ cm}^{-1} \rightarrow 646 \text{ nm}$  (Q band) and  $E_{3,4} = 22\,987 \text{ cm}^{-1} \rightarrow 435 \text{ nm}$  (B band). These transition energies were chosen to match peaks in the experiment at low concentrations ( $c = 3 \times 10^{-6} \text{ mol L}^{-1}$ ) at pH 1,<sup>21</sup> when monomers are expected to dominate the spectra.

Dipole–dipole intermolecular interaction was assumed for off-diagonal elements of the Hamiltonian between different molecules:

$$V_{ni,mj} = k_e \left[ \frac{\boldsymbol{\mu}_{ni} \cdot \boldsymbol{\mu}_{mj}}{\mathbf{R}_{nm}^3} - 3 \frac{(\boldsymbol{\mu}_{mj} \cdot \mathbf{R}_{nm})(\boldsymbol{\mu}_{ni} \cdot \mathbf{R}_{nm})}{\mathbf{R}_{nm}^5} \right], \quad (3)$$

where  $k_e = 4\pi\epsilon\epsilon_0^{-1}$  is the Coulomb interaction constant,  $\boldsymbol{\mu}_{ni}$  and  $\boldsymbol{\mu}_{mj}$  are respectively the  $n$ th and  $m$ th molecules'  $i$ th and  $j$ th optical transition dipole vectors of each molecule, and  $\mathbf{R}_{nm}$  is the vector connecting the  $n$ th and  $m$ th molecules' dipole origins (in calculations it is taken as a vector connecting the center of masses of the nitrogen atoms of specific molecules).  $\mathbf{R}_{nm}$  is the vector length (distance). The transition dipole vectors were assigned values of  $3.9D$  and  $11.6D$  for Q and B bands, respectively. These dipole values were tuned to fit the main features of the experimental results presented in ref. 21.

The matrix of transition dipoles forms the aggregate polarization operator, which can be written in the following form:

$$\hat{P} = \sum_{n=1}^N \sum_{i=1}^4 \boldsymbol{\mu}_{ni} |0\rangle\langle n_i| + \text{h.c.}, \quad (4)$$

where  $|0\rangle$  is the vacuum state with all molecules in their ground state, h.c. is the Hermitian conjugate. This operator is the basis of the response function formulation of the optical spectroscopy theory,<sup>57</sup> hence, absorption and CD spectra. For this purpose, the problem is switched into exciton representation.

The exciton states are calculated by solving the Hamiltonian eigenvalue equation:

$$\hat{H}\psi = \varepsilon\psi, \quad (5)$$

where  $\varepsilon$  is the eigen energy of stationary state  $\psi$ . Given the full set of eigenvectors with corresponding eigenvalues, and using the Gaussian line shape model, the absorption spectrum is given by a sum over the transitions from electronic ground state to each exciton:

$$A(\omega) = \sum_e^{N \times 4} |\mathbf{d}_e|^2 \exp\left(-\frac{(\omega - \varepsilon_e)^2}{2\gamma_e^2}\right), \quad (6)$$

Here  $\omega$  is the frequency (or energy, when  $\hbar = 1$ ) and  $\varepsilon_e$  is the eigenenergy of the associated excitonic state  $e$  in  $\text{cm}^{-1}$ . The Gaussian function represents the Gaussian spectral line shape model, with  $\gamma_e$  being the Gaussian root mean square (RMS) width of the corresponding exciton. To obtain the best fit, we assigned two damping constants:  $\gamma_B = 300 \text{ cm}^{-1}$  was used for the B band and  $\gamma_Q = 500 \text{ cm}^{-1}$  for the Q band.

$\mathbf{d}_e = \sum_{n=1}^N \sum_{i=1}^4 \boldsymbol{\mu}_{ni} \psi_{ni,e}$  is the exciton transition dipole, where  $\psi_{ni,e}$  is the eigenvector component of excitonic state  $e$ . Similarly, the CD spectrum<sup>25,26</sup> is given by:

$$\text{CD}(\omega) = \omega \sum_e^{N \times 4} R_e \exp\left(-\frac{(\omega - \varepsilon_e)^2}{2\gamma_e^2}\right), \quad (7)$$

where:

$$R_e = \varepsilon_e \sum_{mn}^N \sum_{ij}^4 \psi_{ni,e} \psi_{mj,e} \mathbf{R}_{nm} \cdot (\boldsymbol{\mu}_{ni} \times \boldsymbol{\mu}_{mj}), \quad (8)$$

## Conclusions

We performed QM and MM optimization of the  $\text{TPPS}_4$  zwitterionic form (Z1 and Z2) monomers. The GAFF description of these monomers was revised. Several parameters – atom types, bond lengths, valence angles and dihedral angles – were adjusted to improve the description of the Z1 and Z2 structures. Two linear  $\text{TPPS}_4$  Z1 and Z2 tetramers were constructed and their MD simulation was performed. Absorption and CD spectra of these tetramers were also calculated. It was determined that both Z1 and Z2 tetramers form on average a curved chiral structure, *i.e.* the four monomers in tetramers (both Z1 and Z2) do not stay on a perfect line. According to our results, the ring should contain 48 molecules of  $\text{TPPS}_4$  in the cylindrical structures. The Z1-based structure is more straight and more compact.



Accordingly, intermolecular couplings in the Z1 tetramer are larger. A comparison was performed of Z1 and Z2 tetramers' absorption spectra with the measured spectra from a previous published article. Our analysis of results demonstrates that the larger peak shifts of the Z1 tetramer's spectra are more similar to the experimental data; however, other configurations can be possible as well.

## Data availability

The data supporting this article have been included as part of the ESI.<sup>†</sup>

## Author contributions

Laura Baliulyte: writing – original draft (lead); writing – review & editing (equal); visualization (equal); methodology (equal); investigation (equal); formal analysis (equal); conceptualization (equal). Eimantas Urnziejus: writing – original draft (equal); visualization (equal); methodology (equal); investigation (equal); formal analysis (equal). Vytautas Bubilaitis: methodology (supporting); formal analysis (supporting). Mindaugas Macernis: writing – review & editing (supporting). Lorenzo Cupellini: supervision (equal); writing – review & editing (lead); visualization (supporting); methodology (equal); conceptualization (equal). Darius Abramavicius: supervision (lead); writing – original draft (equal), writing – review & editing (lead); methodology (equal); conceptualization (equal); funding acquisition (lead); project administration (lead).

## Conflicts of interest

There are no conflicts of interest to declare.

## Acknowledgements

LB has been partly supported under the Project HPC-EUROPA3 (INFRAIA-2016-1-730897), with the support of the EC Research Innovation Action under the H2020 Programme and the computer resources and technical support provided by CINECA. LB, VB, MM and DA were supported by the Research Council of Lithuania (Grant No. S-MIP-23-48). Most computations were performed using resources at the supercomputer "VU HPC" Saulėtekis of Vilnius University at the Faculty of Physics.

## Notes and references

- B. Hemavathi, V. Jayadev, S. C. Pradhan, G. Gokul, K. Jagadish, G. K. Chandrashekara, P. C. Ramamurthy, R. K. Pai, K. N. N. Unni, T. N. Ahipa, S. Soman and R. G. Balakrishna, *Sol. Energy*, 2018, **174**, 1085–1096.
- J. L. Banal, B. Zhang, D. J. Jones, K. P. Ghiggino and W. W. H. Wong, *Acc. Chem. Res.*, 2017, **50**(1), 49–57.
- G. G. Parra, D. S. Correa, E. Silveira-Alves, L. M. Almeida, M. A. R. Souza, L. De Boni, L. Misoguti, C. R. Mendonça, *Spectrochim. Acta, Part A*, 2021, **261**, 120063.

- S. Kwiatkowski, B. Knap, D. Przystupski, J. Saczko, E. Kędzierska, K. Knap-Czop, J. Kotlińska, O. Michel, K. Kotowski and J. Kulbacka, *Biomed. Pharmacother.*, 2018, **106**, 1098–1107.
- Y. Ferro, S. Maurotti, M. G. Tarsitano, O. Lodari, R. Pujia, E. Mazza, L. Lascala, R. Russo, A. Pujia and T. Montalcini, *Nutrients*, 2023, **15**, 2666.
- L. Barazzuol, R. P. Coppes and P. van Luijk, *Mol. Oncol.*, 2020, **14**(7), 1538–1554.
- M. A. Castricano, A. Romeo, V. Villari, N. Micali and L. M. Scolaro, *J. Phys. Chem. B*, 2003, **107**(34), 8765–8771.
- T. Kim, S. Ham, S. H. Lee, Y. Hong and D. Kim, *Nanoscale*, 2018, **10**(35), 16438–16446.
- L. P. F. Aggarwal and I. E. Borishevitch, *Spectrochim. Acta, Part A*, 2006, **63**(1), 227–233.
- I. G. Occhiuto, R. Zagami, M. Trapani, M. A. Castricano, A. Romeo and L. M. Scolaro, *Molecules*, 2020, **25**(23), 5742.
- J. M. Short, J. A. Berriman, C. Kübel, Z. El-Hachemi, J. V. Naubron and T. S. Balaban, *ChemPhysChem*, 2013, **14**(14), 3209–3214.
- R. Rotomskis, R. Augulis, V. Snitka, R. Valiokas and B. Liedberg, Hierarchical structure of TPPS4 J-aggregates on substrate revealed by atomic force microscopy, *J. Phys. Chem. B*, 2004, **108**(9), 2833–2838.
- G. Pescitelli, L. Di Bari and N. Berova, *Chem. Soc. Rev.*, 2014, **43**, 5211–5233.
- T. Kobayashi, *J-Aggregates*, World Scientific Publishing Company, Singapore, 1996.
- Y. Xiu, X. Zhang, Y. Feng, R. Wei, S. Wang, Y. Xia, M. Cao and S. Wang, *Nanoscale*, 2020, **12**(28), 15201–15208.
- R. Augulis, J. Tamuliene, A. Tamulis and R. Rotomskis, *Solid State Phenom.*, 2004, **97**, 225–228.
- M. Pleckaitis, F. Habach, L. Kontenis, G. Steinbach, G. Jarockyte, A. Kalnaityte, I. Domonkos, P. Akhtar, M. Alizadeh, S. Bagdonas, V. Karabanovas, G. Garab, R. Rotomskis and V. Barzda, *Nano Res.*, 2022, **15**(6), 5527–5537.
- F. Sabuzi, M. Stefanelli, D. Monti, V. Conte and P. Galloni, *Molecules*, 2019, **5**(1), 133.
- G. G. B. Alves, F. C. Lavarda, C. F. O. Graeff and A. Batagin-Neto, *J. Mol. Graphics Model.*, 2020, **98**, 107609.
- K. Ishii, S. Hattori and Y. Kitagawa, *Photochem. Photobiol. Sci.*, 2020, **19**(1), 8–19.
- L. Baliulyte, D. Abramavicius, S. Bagdonas, A. Kalnaityte, V. Poderys, R. Rotomskis and V. Barzda, *AIP Adv.*, 2023, **13**(10), 105011.
- S. Bottaro and K. Lindorff-Larsen, *Science*, 2018, **361**, 355–360.
- S. Maity and U. Kleinekathöfer, *Photosynth. Res.*, 2023, **156**(1), 147–162.
- G. Schifino, M. Fortino, L. M. Scolaro and A. Pietropaolo, *Mol. Syst. Des. Eng.*, 2023, **8**(12), 1512–1519.
- F. Bertocchi, C. Sissa and A. Painelli, *Chirality*, 2023, **35**(10), 681–691.



26 L. D. Barron, *Molecular Light Scattering and Optical Activity*, Cambridge University Press, 2004.

27 J. Wang, W. Wang, P. A. Kollman and D. A. Case, *J. Am. Chem. Soc.*, 2001, **222**, 2001.

28 F. Guerra, S. Adam and A. N. Bondar, *J. Mol. Graphics Modell.*, 2015, **58**, 30–39.

29 Z. El-Hachemi, C. Escudero, F. Acosta-Reyes, M. T. Casas, V. Altoe, S. Aloni, G. Oncins, A. Sorrenti, J. Crusats, J. L. Campos and J. M. Ribó, *J. Mater. Chem. C*, 2013, **1**(20), 3337–3346.

30 S. M. Vlaming, R. Augulis, M. C. A. Stuart, J. Knoester and P. H. M. Van Loosdrecht, *J. Phys. Chem. B*, 2009, **113**(8), 2273–2283.

31 L. Zhang, D. A. Silva, Y. Yan and X. Huang, *J. Comput. Chem.*, 2012, **33**(25), 1969–1980.

32 O. Ohno, Y. Kaizu and H. Kobayashi, *J. Chem. Phys.*, 1993, **99**(5), 4128–4139.

33 A. S. R. Koti, J. Taneja and N. Periasamy, *Chem. Phys. Lett.*, 2003, **375**(1–2), 171–176.

34 R. Randazzo, M. Gaeta, C. M. A. Gangemi, M. E. Fragalà, R. Purrello and A. D'Urso, *Molecules*, 2019, **24**(1), 84.

35 M. A. Castricano, D. Gentili, A. Romeo, M. Cavallini and L. M. Scolaro, *Sci. Rep.*, 2017, **7**, 44094.

36 L. Zeng, Y. He, Z. Dai, J. Wang, Q. Cao and Y. Zhang, *ChemPhysChem*, 2009, **10**(6), 954–962.

37 A. D'Urso, R. Randazzo, L. L. Faro and R. Purrello, *Angew. Chem., Int. Ed.*, 2010, **49**(1), 108–112.

38 A. Romeo, M. A. Castricano, I. Occhiuto, R. Zagami, R. F. Pasternack and L. M. Scolaro, *J. Am. Chem. Soc.*, 2014, **136**(1), 40–43.

39 G. Occhiuto, R. Zagami, M. Trapani, L. Bolzonello, A. Romeo, M. A. Castricano, E. Collini and L. M. Scolaro, *Chem. Commun.*, 2016, **52**(77), 11520–11523.

40 T. Renger and F. Müh, *Photosynth. Res.*, 2012, **111**, 47–52.

41 U. Mazur and K. W. Hipps, *J. Phys. Chem. C*, 2018, **122**(40), 22803–22820.

42 R. Dennington, T. A. Keith and J. M. Millam, *GaussView, Version 6.1*, Semichem Inc., Shawnee Mission, KS, 2016.

43 R. E. Skyner, J. L. McDonagh, C. R. Groom, T. van Mourik and J. B. O. Mitchell, *Phys. Chem. Chem. Phys.*, 2015, **17**(9), 6174–6191.

44 M. J. Frisch, G. W. Trucks, H. B. Schlegel, G. E. Scuseria, M. A. Robb, J. R. Cheeseman, G. Scalmani, V. Barone, G. A. Petersson, H. Nakatsuji, X. Li, M. Caricato, A. V. Marenich, J. Bloino, B. G. Janesko, R. Gomperts, B. Mennucci, H. P. Hratchian, J. V. Ortiz, A. F. Izmaylov, J. L. Sonnenberg, D. Williams-Young, F. Ding, F. Lipparini, F. Egidi, J. Goings, B. Peng, A. Petrone, T. Henderson, D. Ranasinghe, V. G. Zakrzewski, J. Gao, N. Rega, G. Zheng, W. Liang, M. Hada, M. Ehara, K. Toyota, R. Fukuda, J. Hasegawa, M. Ishida, T. Nakajima, Y. Honda, O. Kitao, H. Nakai, T. Vreven, K. Throssell, J. A. Montgomery, Jr., J. E. Peralta, F. Ogliaro, M. J. Bearpark, J. J. Heyd, E. N. Brothers, K. N. Kudin, V. N. Staroverov, T. A. Keith, R. Kobayashi, J. Normand, K. Raghavachari, A. P. Rendell, J. C. Burant, S. S. Iyengar, J. Tomasi, M. Cossi, J. M. Millam, M. Klene, C. Adamo, R. Cammi, J. W. Ochterski, R. L. Martin, K. Morokuma, O. Farkas, J. B. Foresman and D. J. Fox, *Gaussian 16, Revision C.01*, Semichem Inc., Shawnee Mission, KS, 2016.

45 J. Wang, R. M. Wolf, J. W. Caldwell, P. A. Kollman and D. A. Case, *J. Comput. Chem.*, 2004, **25**(9), 1157–1174.

46 M. A. González, Force fields and molecular dynamics simulations, *Collection SFN*, 2011, **12**, 169–200.

47 C. I. Bayly, P. Cieplak, W. D. Cornell and P. A. Kollman, *J. Phys. Chem.*, 1993, **97**(40), 10269–10280.

48 J. Wang, W. Wang, P. A. Kollman and D. A. Case, *J. Mol. Graphics Modell.*, 2006, **25**(2), 247–260.

49 D. A. Case, H. M. Aktulga, K. Belfon, I. Y. Ben-Shalom, J. T. Berryman, S. R. Brozell, D. S. Cerutti, T. E. Cheatham, III, G. A. Cisneros, V. W. D. Cruzeiro, T. A. Darden, R. E. Duke, G. Giambasu, M. K. Gilson, H. Gohlke, A. W. Goetz, R. Harris, S. Izadi, S. A. Izmailov, K. Kasavajhala, M. C. Kaymak, E. King, A. Kovalenko, T. Kurtzman, T. S. Lee, S. LeGrand, P. Li, C. Lin, J. Liu, T. Luchko, R. Luo, M. Machado, V. Man, M. Manathunga, K. M. Merz, Y. Miao, O. Mikhailovskii, G. Monard, H. Nguyen, K. A. O'Hearn, A. Onufriev, F. Pan, S. Pantano, R. Qi, A. Rahnouni, D. R. Roe, A. Roitberg, C. Sagui, S. Schott-Verdugo, A. Shajan, J. Shen, C. L. Simmerling, N. R. Skrynnikov, J. Smith, J. Swails, R. C. Walker, J. Wang, J. Wang, H. Wei, R. M. Wolf, X. Wu, Y. Xiong, Y. Xue, D. M. York, S. Zhao and P. A. Kollman, *Amber 2022*, University of California, San Francisco, 2022.

50 S. Izadi, R. Anandakrishnan and A. V. Onufriev, *J. Phys. Chem. Lett.*, 2014, **5**(21), 3863–3871.

51 R. Augulis, V. Snitka and R. Rotomskis, *Solid State Phenom.*, 2004, **97**, 191–194.

52 V. Snitka, M. Rackaitis and R. Rodaite, *Sens. Actuators, B*, 2005, **109**(1), 159–166.

53 T. Darden, L. Perera, L. Li and P. Lee, *Structure*, 1999, **7**(3), R55–R60.

54 D. R. Roe and T. E. Cheatham, *J. Chem. Theory Comput.*, 2013, **9**(7), 3084–3095.

55 W. Humphrey, D. Andrew and S. Klaus, *J. Mol. Graphics*, 1996, **14**(1), 33–38.

56 J. M. Ribó, J. M. Bofill, J. Crusats and R. Rubires, *Chem. – Eur. J.*, 2001, **7**(13), 2733–2737.

57 S. Mukamel, *Principles of Nonlinear Optical Spectroscopy*, Oxford University Press, New York, 1995.

